Journal of
Materials Chemistry C

ROYAL SOCIETY
OF CHEMISTRY

PAPER

View Article Online
View Journal | View Issue

Check for updates

Cite this: *J. Mater. Chem. C*, 2025, 13, 393

Boosting the light-driven pyroelectric response of poly(vinylidene difluoride) by constructing Mn-doped BZT-BCT/PVDF composites†

Lu Wang,[a] Feilong Yan,[c] Jifeng Pan,[a] Xiang He,[a] Chen Chen,[a] Muzaffar Ahmad Boda[a] and Zhiguo Yi*[ab]

Received 17th June 2024,
Accepted 24th October 2024

DOI: 10.1039/d4tc02514h

rsc.li/materials-c

Poly(vinylidene difluoride) (PVDF) with lightweight and mechanically flexible features is prevalently used in designing pyroelectric photodetectors. However, the generated electrical signals are often limited by its low pyroelectric coefficient. In this work, Mn-doped BZT-BCT (BZTM$_{0.12}$-BCT) particles with a narrow bandgap and a high pyroelectric coefficient are introduced into a PVDF film to enhance its photo-pyroelectric response. The addition of BZTM$_{0.12}$-BCT positively impacts the content of the electroactive phase, crystallinity and photothermal conversion capability. These factors jointly enhance the photo-pyroelectric response. The PVDF composite film with a BZTM$_{0.12}$-BCT content of 10 wt% presents an optimal photo-pyroelectric current, about 30 times higher than that of the pure PVDF film. Besides, the composite film shows excellent visible response from 365 nm to 660 nm light zones and superior maintenance over 71% under great bending conditions and almost 100% under repeated periodic illuminations after 100 cycles. Furthermore, it is easy to control the amplitude and waveform of the output signals simply by regulating the frequency of the periodic illuminations, showing critical potential in the complex and changeable environments. This work provides a simple strategy to improve the photo-pyroelectric output of the PVDF film, making it a potential candidate for future self-powered applications.

1. Introduction

Signal recognition plays an important role in the advancement of intelligent society.[1–3] The use of light as an important information carrier and green energy has been extensively explored in recent decades.[4–7] Self-powered photodetectors without any external power supply to realize device miniaturization and integration are critical for the implementation of smart systems.[8,9] The well-controlled switchable polarization of ferroelectric materials enables the conversion of photo signals into electrical signals *via* the photo-induced pyroelectric effect.[10–12] When applying or withdrawing light, the temperature change results in the polarization fluctuation in ferroelectric materials, causing bound charges to flow through an external circuit and generate current. Due to unique advantages, including broadband photo response, programmable designing, and low power consumption, pyroelectric photodetectors show obvious superiority in many fields such as remote control and Internet-of-Things (IoT).[1,13–15]

Poly(vinylidene difluoride) (PVDF), known for its lightweight, mechanical flexibility and biocompatibility, has developed markedly in pyroelectric devices.[16–18] However, because of the high-content nonpolar α phase, the pyroelectric coefficient ρ of pure PVDF film is far lower than that of inorganic ferroelectrics, which inhibits the magnitude of pyroelectric response. According to the equation for pyroelectric current:[19]

$$I_{\mathrm{py}} = \rho \cdot A \cdot \left(\frac{\mathrm{d}T}{\mathrm{d}t}\right) \tag{1}$$

where A and $\mathrm{d}T/\mathrm{d}t$ are the effective electrode area and temperature change rate, respectively. The output I_{py} can be enhanced by improving ρ or $\mathrm{d}T/\mathrm{d}t$. For example, embedding inorganic ferroelectric materials into an organic film can obviously increase the content of polar β phase, thus boosts ρ strikingly.[20–23] In addition, carbon-based electrodes and patterning electrodes have been developed to substantially enhance $\mathrm{d}T/\mathrm{d}t$.[14,24–26] Intuitionally, the simultaneous improvements of both ρ and $\mathrm{d}T/\mathrm{d}t$ are more helpful

---

[a] *State Key Laboratory of High Performance Ceramics and Superfine Microstructure, Shanghai Institute of Ceramics, Chinese Academy of Sciences, Shanghai 200050, China. E-mail: zhiguo@mail.sic.ac.cn*

[b] *Center of Materials Science and Optoelectronics Engineering, University of Chinese Academy of Sciences, Beijing 100049, China*

[c] *Key Laboratory of Optoelectronic Material and Device, Department of Physics, Shanghai Normal University, Shanghai 200234, China*

† Electronic supplementary information (ESI) available. See DOI: **https://doi.org/10.1039/d4tc02514h**

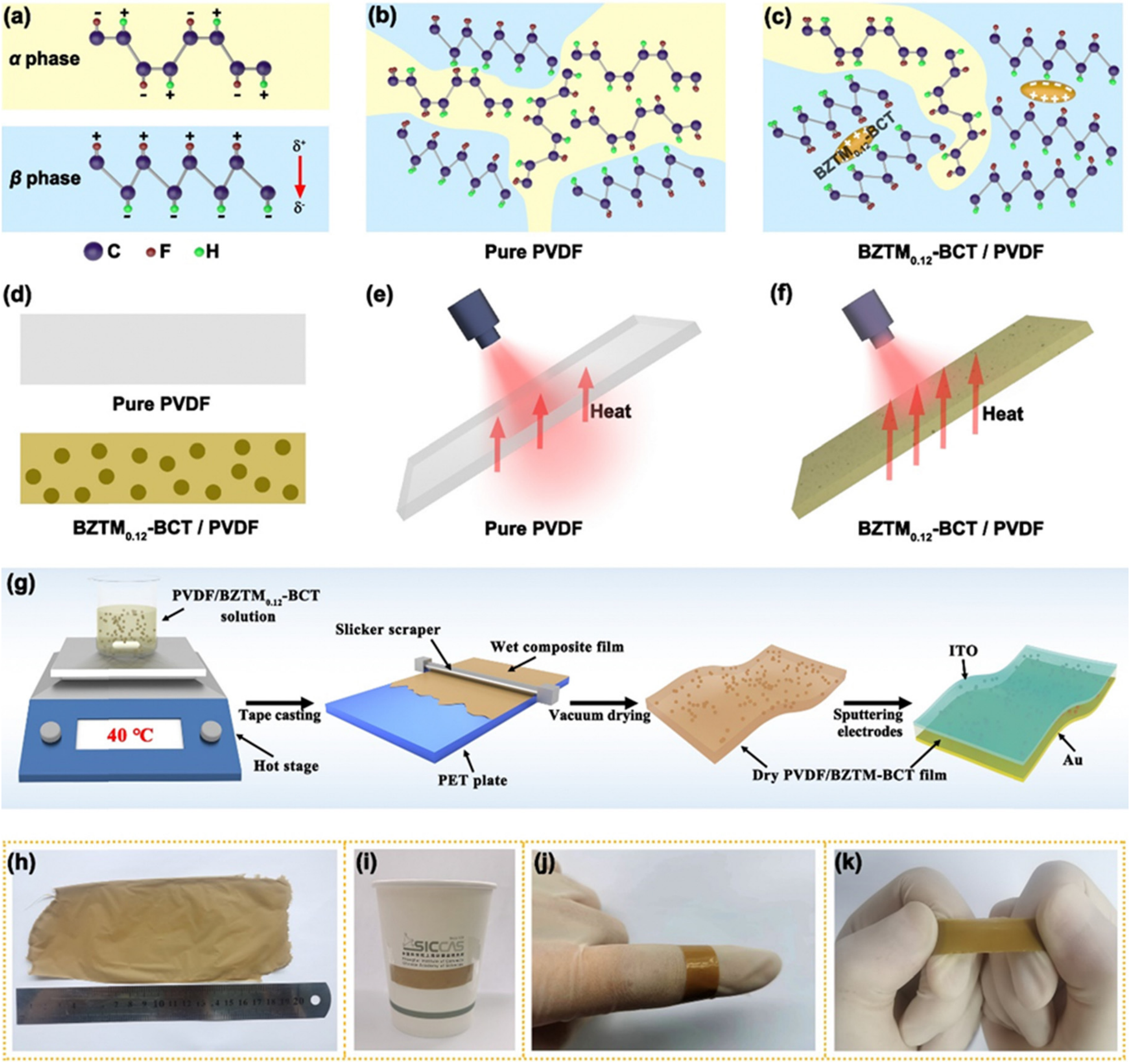

Fig. 1 Scheme design, preparing processes and exhibition of the PVDF-*x* composite films. (a–f) Schematic diagram enhancing the polar phase content (a–c) and photo-absorption (d–f) by adding BZTM0.12-BCT particles into PVDF. (g) Preparation processes of the PVDF-*x* composite films. (h–k) Measurement of the (h) size, (i) and (j) flexible properties and (k) tearing resistance performance of PVDF-*x* composite films.

to enhance the pyroelectric output. However, the direct combination of the two above-mentioned strategies will increase the complexity of the preparation procedure, and the relevant research is rarely studied.

In previous research, we have reported a new narrow bandgap ferroelectric ceramic comprising $0.5Ba(Zr_{0.08}Ti_{0.8}Mn_{0.12})O_3$–$0.5(Ba_{0.7}Ca_{0.3})TiO_3$ ($BZTM_{0.12}$-BCT) with a Curie temperature of about 66 °C.[27] Fig. S1 and S2 (ESI†) show its X-ray diffraction spectrum and UV-vis spectrum, indexing to the tetragonal phase of $BaTiO_3$. Compared with the traditional wide bandgap ferroelectrics, the $BZTM_{0.12}$-BCT composition presents excellent photothermal conversion ability and large pyroelectric coefficient ($\sim$58.3 nC cm^2 K^{-1}), but the natural rigidity restricts its applications. Hence, we constructed the $BZTM_{0.12}$-BCT/PVDF composite films with increasing polar phase content and photothermal conversion ability to achieve a win–win situation (Fig. 1a–f). Exactly, the feasibility of such strategy is confirmed. The addition of $BZTM_{0.12}$-BCT particles notably boosts the photo-pyroelectric current, about 30 times higher than that of the pure PVDF film. More interestingly, the photo-pyroelectric output presents excellent stability and practicable amplitude and waveform controllability by modulating the light irradiation frequency.

2. Experimental section

2.1 Fabrication of PVDF/$BZTM_{0.12}$-BCT films

The $Ba(Zr_{0.08}Ti_{0.8}Mn_{0.12})O_3$–$(Ba_{0.7}Ca_{0.3})TiO_3$ ($BZTM_{0.12}$-BCT) ceramic particles were pre-calcined by a solid-state reaction method. The experimental details have been presented in our previous study.[27] The poly(vinylidene fluoride) (PVDF) films embedded with different contents of BZTM$_{0.12}$-BCT (x%BZTM$_{0.12}$-BCT/PVDF abbreviated as PVDF-x, x = 0, 5, 10, 15, and 20) were fabricated by a simple tape casting method. First, the BZTM$_{0.12}$-BCT particles were evenly dispersed in *N*,*N*-dimethylformamide (DMF) under continuous stirring at room temperature for 2 h. Then, the PVDF powders were added into the suspension, and the weight ratio of PVDF/DMF was 1/10. The mixture was stirred continuously at 40 °C for 6 h to make the PVDF powders dissolve and completely remove the bubbles. Immediately, the uniformly distributed suspension was poured onto a polyethylene terephthalate (PET) film to tape cast a uniform film. The wet films were heated at 40 °C in vacuum for 3 h to evaporate the DMF solvent and reduce the stomas. Lastly, the films were annealed at 120 °C for 2 h to increase the crystallinity.

2.2 Fabrication of flexible photo-pyroelectric devices

The obtained PVDF/BZTM$_{0.12}$-BCT composite films were tailored to squares with dimensions of 2 × 2 cm^2. The ITO and Au electrodes with sizes of 1.5 × 1.5 cm^2 were deposited on both the surfaces of films by RF magnetron sputtering and vacuum evaporation, respectively (Fig. S3, ESI†). Subsequently, the devices were poled at 100 MV m^{-1} for 30 min in silicon oil.

2.3 Characterization and measurement

The microstructure and morphology of the ceramic powders and films were observed using a field emission scanning electron microscope (FESEM, ZEISS GeminiSEM 300, Germany). The phase structure was measured using an X-ray diffractometer (XRD, Bruker D8 ADVANCE, Germany) with

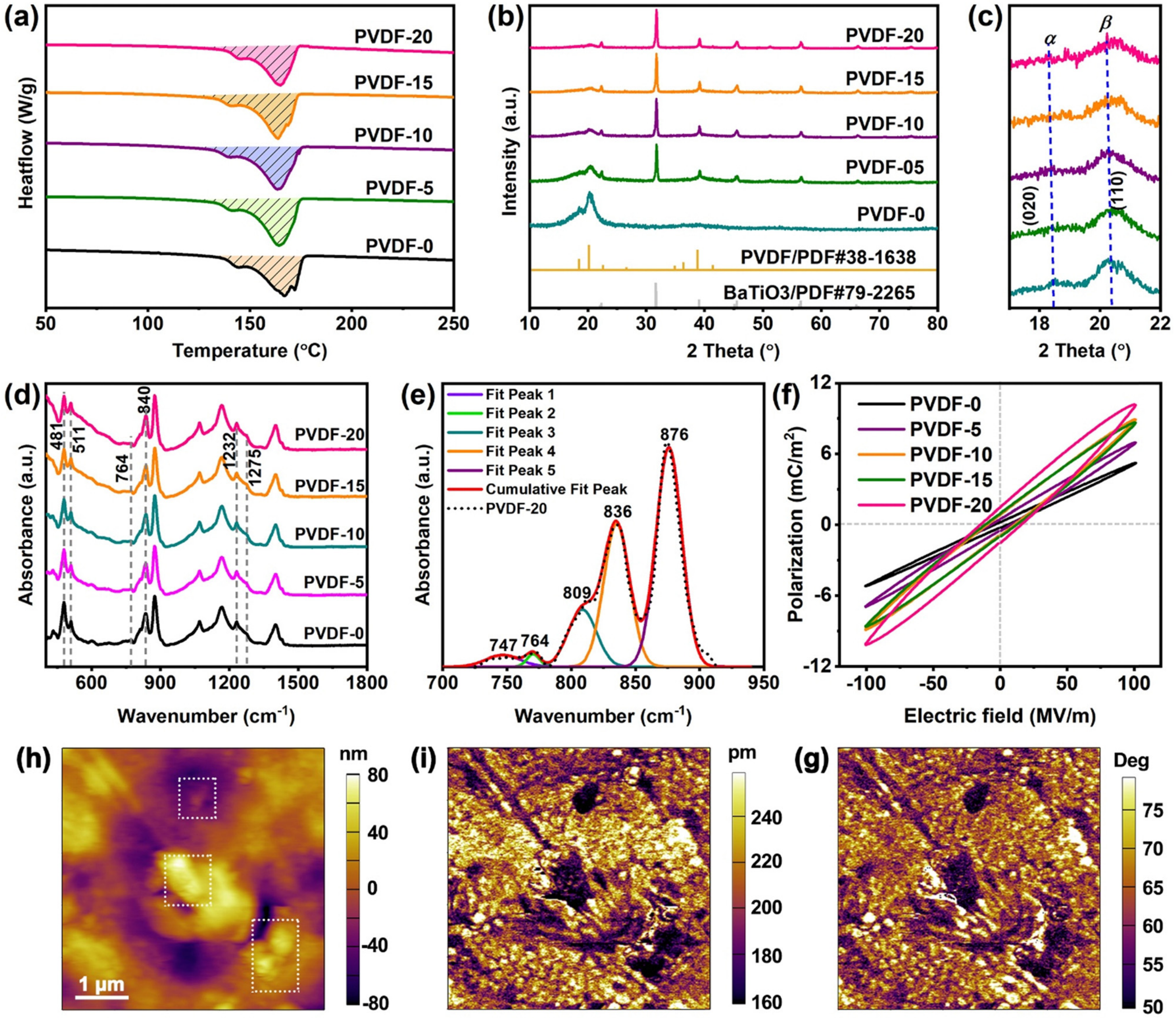

Fig. 2 Polar related characterization of PVDF-x films. (a) DSC curves. (b) XRD patterns. (c) Enlarged parts of 2 theta from 17° to 22° in (b). (d) FTIR spectra. (e) Fitting curves of FTIR of PVDF-20 films from 700 to 950 cm^{-1} in (d). (f) Polarization–electric field curves. (h–g) Out-of-plane PFM height (h), amplitude (i), and phase (g) images of the PVDF-10 film.

Cu-K_α radiation. Additionally, a Fourier transform infrared (FTIR) spectrometer (Thermo Fisher Scientific Nicolet iS50R, USA) was also used to analyze the crystalline phase as well as the phase ratio of the composite films. The crystallinity was calculated by differential scanning calorimetry (DSC, NETZSCH, STA449C, Germany). The photo absorption and transmission were tested using a PerkinElmer Lambda 900 UV-vis-NIR spectrometer. The piezoelectric response was tested using a piezoelectric force microscope (PFM, MFP-3D, USA). The ferroelectric properties were measured using a ferroelectric testing system (TF2000E analyzer, axiACCT, Germany). The temperature variations of the photoelectric devices under different light illumination conditions were monitored using an infrared thermal image instrument and a thermocouple module. The photoelectric response of the poled film devices was monitored using a high precision electrometer (Keithley 6517B). The used lights were LEDs with different wavelengths of 365, 405, 450, 520 and 660 nm.

3. Results and discussion

3.1. Structural and physical properties

Fig. 1g schematically illustrates the preparing processes of the x%$BZTM_{0.12}$-BCT/PVDF (abbreviated as PVDF-x) composite films by a tape casting method. This method is prevalent and convenient. The thicknesses of the obtained films are almost 20 μm (Fig. S4, ESI†). As shown in Fig. 1h–k, the size of the films is easily scaled up, depending on the sizes of the PET substrate and the scraper. For some things, like paper cup and fingers, the films are highly conformal. Moreover, the films exhibit good tearing resistance. All these exhibitions suggest the excellent flexibility and mechanical properties of the composite films.

The DSC thermogram curves were tested to estimate the film quality (Fig. 2a). The melting point of PVDF-x films is about 165.6 °C. The crystallinity (X_C) can be determined by the ratio between the melting enthalpy (ΔH_m) of the composite films and the theoretical enthalpy (ΔH_m^0) of the pure PVDF film with 100% crystallinity, as follows:[22]

$$X_C = \frac{\Delta H_m}{(1-\varphi)\Delta H_m^0} \tag{2}$$

where φ is the mass percentage of $BZTM_{0.12}$-BCT particles in the composite film. The value of ΔH_m^0 is 104.6 J g^{-1}. As listed in Table S1 (ESI†), the PVDF-10 film exhibits the maximum crystallinity. When the content of $BZTM_{0.12}$-BCT exceeds 10 wt%, the crystallinity gradually decreases with the increase in x. This is mainly caused by the poor quality of the films with high contents of $BZTM_{0.12}$-BCT powders. As shown in Fig. S5 (ESI†), the granule size of the $BZTM_{0.12}$-BCT particles is about 1 μm. These particles are well distributed and embedded into the PVDF films. Therefore, the pure PVDF, PVDF-5, and PVDF-10 films present dense and smooth surfaces. However, these particles become aggregated in PVDF-15 and PVDF-20, resulting in the occurrence of pores and aggregation. These affect the composite film quality. Combining with the intrinsically weaker breakdown electric field of inorganic ferroelectric materials than PVDF, the breakdown electric fields of the films decrease after introducing BZTM-BCT particles. Especially when the BZTM-BCT content exceeds 10%, it rapidly declines, changing from ∼220 MV m^{-1} of PVDF-0 to ∼100 MV m^{-1} of PVDF-20 films (Fig. S6, ESI†).

PVDF is a kind of material with multiple phase structures including α, β, γ, δ and ε phases; among them, α and β phases are the uppermost phases.[28,29] As shown in Fig. 1a, the polarity of PVDF depends on the arrangement modes between $-CH_2-$ and $-CF_2-$ chains.[30,31] Compared with the symmetrical structure in the α phase, the oriented dipole moments in the β phase are arranged in parallel, leading to the polar feature. Experimentally, the phase structure of the prepared PVDF-x composite films was confirmed using an X-ray diffractometer (XRD) (Fig. 2b and c). The peaks at 18.41° and 20.32°, corresponding to the (020) and (110) crystal planes, are obvious indications of the α and β phases, respectively.[28] Thanks to the spontaneous polarization, the electric dipoles of the embedded $BZTM_{0.12}$-BCT particles induce the occurrence of more β phases, confirmed by the enhancing (110)/(020) peak intensity ratio (Fig. S7, ESI†). The content of BZTM-BCT particles may reach percolation threshold in the range from 10% to 15%, resulting in significantly increasing β phase content.[32]

The phase structures were further analyzed using a Fourier transform infrared (FTIR) Spectrometer (Fig. 2d). The absorption bands at 481 and 764 cm^{-1} are the characteristic bands of α phase. In addition, the bands at 1232 and 1275 cm^{-1} are the exclusive bands of electroactive γ and β phases, respectively, while 511 and 840 cm^{-1} are common to the both phases.[28,33] However, some unique features belonging to the γ phase, such as characteristic peaks at 20.04° in the XRD spectra and melting temperature around 179–180 °C, cannot be observed, which indicates that the β phase is dominant in PVDF composite films.[34–36] Using eqn (3), where assuming that the γ phase is negligible, the fraction of electroactive phase F_{EA} in the films can be calculated as follows:[37,38]

$$F_{EA} = \frac{A_{\beta+\gamma}}{\left(\frac{K_\beta}{K_\alpha}\right)A_\alpha + A_{\beta+\gamma}} \tag{3}$$

where A_α and $A_{\beta+\gamma}$ are the peak areas of 764 cm^{-1} and 836 cm^{-1}, respectively. K_α and K_β are two absorptivity constants, equal to 6.1×10^4 cm^2 mol^{-1} and 7.7×10^4 cm^2 mol^{-1}, respectively. The peaks from 700 to 950 cm^{-1} are fitted to obtain A_α and $A_{\beta+\gamma}$ (Fig. 2e). As summarized in Table S1 (ESI†), F_{EA} increases from 81.6% to 92.8% with the increase in x from PVDF-0 to PVDF-20, showing a high content of the ferroelectric phase. As a result, the PVDF film with more BZTM-BCT particles is more inclined to saturate under the same polarized electric field (Fig. 2f and Fig. S8, ESI†). Fig. 2h–g present the out-of-plane piezoresponse of the PVDF-10 film performed by PFM. The ceramic particles are observed from the height image, encircled by squares. The contracts of the BZTM-BCT particles about amplitude and phase signals are obviously darker than the PVDF matrix, indicating more downwardly oriented polarization components in BZTM-BCT particles. In addition, the PVDF component around the BZTM$_{0.12}$-BCT particles shows brighter amplitude and phase contrasts than that away from the particles, further verifying more induced ferroelectric phase by the polar ceramic particles and more obvious piezoelectric response in the PVDF component.[39,40]

3.2. Photo-pyroelectric properties

According to eqn (1), the photothermal conversion ability of the films plays an important role in the photo-pyroelectric response. Under light illumination, partial absorbed photons interact with the crystal lattice, promoting lattice vibration and the generation of heat. Besides, the excited electrons partially jump back into the valence band, which releases heat.[13] Therefore, increasing photo absorption will significantly boost the photothermal conversion ability, *i.e.*, dT/dt. The temperature change ΔT and photo-pyroelectric current I_{py} were measured under a 365 nm LED light of 100 mW cm^{-2} to confirm the superiority of the PVDF-x films. The ΔT value was firstly measured using an infrared image instrument (Fig. S9, ESI†). Obviously, under consistent light irradiation, the more BZTM$_{0.12}$-BCT particles are embedded, the greater ΔT of the films. The maximum temperature presents little difference at a higher content of BZTM$_{0.12}$-BCT. This is also confirmed by the time-dependent temperature change, measured using a time-resolved thermocouple module (Fig. 4a and b). The ΔT value of the PVDF-0 film is about 5.7 °C, and it increases to 7.6 °C of the PVDF-10 film, corresponding to an enhancement of about 50% of maximum dT/dt. With further embedding the BZTM$_{0.12}$-BCT particles, the ΔT and maximum dT/dt only slightly changes. This is strongly related to the change in light absorption. It can be observed that the photo-absorption coefficient increases greatly after introducing few BZTM-BCT particles (<10 wt%), while slowly changes when embedding more BZTM-BCT particles. I_{py} reflects a more obvious change (Fig. 4c). The PVDF-10 film exhibits maximum I_{py} of over 6 nA, 30 times higher than that of the pure PVDF film (below 0.2 nA). Obviously, the enhanced dT/dt is not enough to support such a high improvement in I_{py}. In our previous report, the BZTM$_{0.12}$-BCT composition has been proved to have a high pyroelectric coefficient of 5.83 × 10^{-8} C cm^{-1} K^{-1},[27] which is far higher than 4 × 10^{-9} C cm^{-1} K^{-1} of the pure PVDF. We can reasonably speculate that ρ of the PVDF film is significantly improved by the introduction of the BZTM$_{0.12}$-BCT particles. Therefore, it is the simultaneous improvements of dT/dt and ρ that boost the enhancement of the photo-pyroelectric current. However, I_{py} gradually decreases when the BZTM$_{0.12}$BCT content exceeds 10 wt%. This can be ascribed to the degraded quality of the PVDF-x films (x > 10). The light-induced pyroelectric response mechanism is explained in Fig. S10 (ESI†). When light turns on, the polar dipoles are disturbed and polarization decreases due to the increase in film temperature. Thereby, the bound charges are released from the film surface to form positive peak currents. Oppositely, the polarization increases when light turns off, more free charges flow to film, resulting in negative peak currents. The light wavelength dependence tests exhibit obvious response of the PVDF-10 film under visible light region (Fig. 4d). Because stronger photo absorption will lead to intensified lattice vibration, improving the photothermal conversion ability,[13] temperature change (Fig. S11, ESI†) and photo-pyroelectric response slightly declines with the increase in light wavelength from 365 to 660 nm, similar to the photo-absorption coefficient change with light wavelength (Fig. 3b). The excellent response to visible light is very meaningful in the imaging technique, healthcare industry and so on. In sharp contrast, the pure PVDF film shows very weak response under lights of any wavelength (Fig. S12, ESI†). The optical responsiveness and optical detectivity of PVDF-10 are listed in Table S2 (ESI†). Self-powered feature, flexibility and broadband light response make the PVDF/BZTM-BCT composite film superior to traditional photodetectors. Concurrently, it shows output current as large as those PVDF-based films tested under higher light intensities, indicating great pyroelectric response (Table S3, ESI†).

The frequency characteristics of the pyroelectric devices deserve study to achieve the applications in different conditions such as environment monitoring, healthcare industries

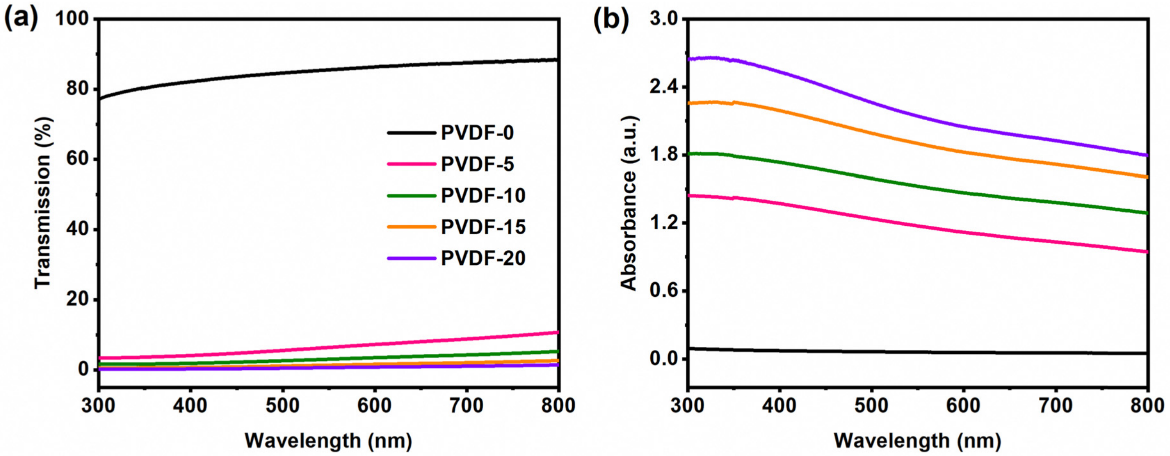

Fig. 3 Photo-absorption properties of the PVDF-*x* films. (a) Transmission and (b) absorbance.

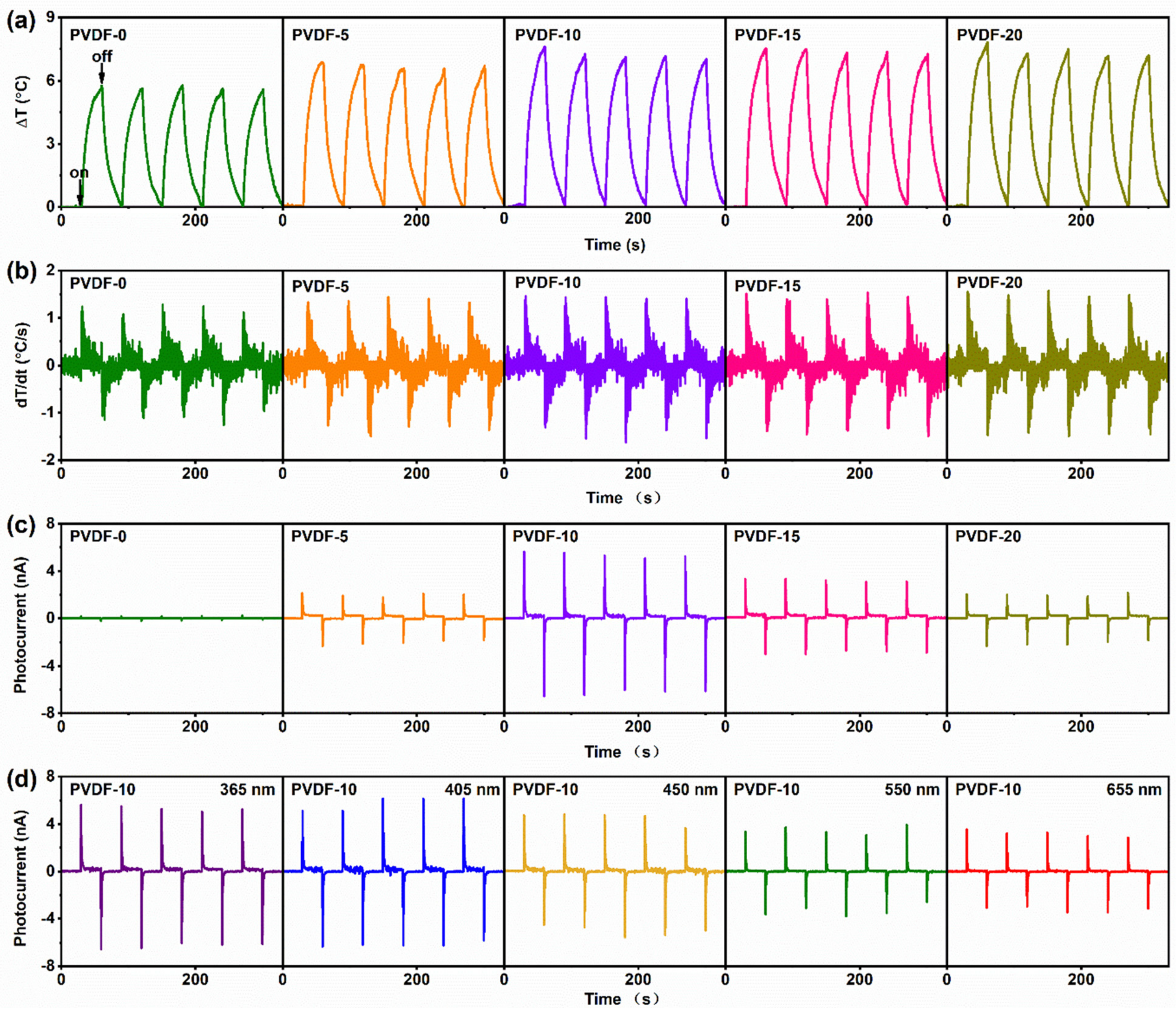

Fig. 4 Comparative analyses of photo-induced temperature variation and pyroelectric current of different films. (a) Temperature changes ΔT, (b) temperature change rate dT/dt and (c) photo-pyroelectric currents I_{py} of different films under periodic 365 nm LED light irradiation of 100 mW cm^{-2}, tested by a thermocouple module. (d) Photo-pyroelectric response of PVDF-10 films under light with different wavelengths.

and photodetections.[14,26,41] Three different periodic light illumination conditions are used to discuss the photo-pyroelectric output dependence on the light turning on/off time (Fig. 5a–c). During this discussion, it's should be noted that the output voltage (V_{oc}) needs longer time than the output current to show more accurate V_{oc} evolution, so the testing time for I_{py} and V_{oc} is different under every periodic light irradiation.

In situation (i): the time spans of the light turning on (t_{on}) and turning off (t_{off}) are identical (Fig. 5a). Whatever the period, the positive I_{py} always reaches the maximum of about 6 nA at the beginning of the period, and then, with continuous periodic irradiation, the positive and negative I_{py} start to decrease and increase respectively, and finally become stable (Fig. 5d). The magnitude of stable I_{py} gradually increases from 3.8 nA to 6.0 nA with extending t_{on} and t_{off} from 0.1 s to 2.0 s. The dT/dt presents consistent change with I_{py} (Fig. S13, ESI†), indicating the close relationship between I_{py} and dT/dt of the film under periodic illumination. At the beginning of the periodic illumination, when the film temperature is low, once the light illuminates, the temperature rises rapidly. However, during the light off, the heat dissipation is slow due to the small difference between the film and the environment. Therefore, the film has a net temperature increase and presents large positive I_{py} but small negative I_{py} at the initial periodic illumination. As the periodic illumination continued, the film temperature gradually increases, slowing down the speed of temperature increase when the light is on but speeding up the temperature decrease when the light is off. Ultimately, the film temperature becomes stable and the temperature change achieves a dynamic balance under periodic illumination. Consequently, the positive/negative I_{py} decrease/increase and then remain unchanged. The longer the period, the greater the temperature disturbance and the greater the stable I_{py}. As for the output voltage, because the positive I_{py} is far larger than the negative I_{py} at the initial period, the charges flowing into and out of the film are not equal, making the generated output voltage fail to restore to

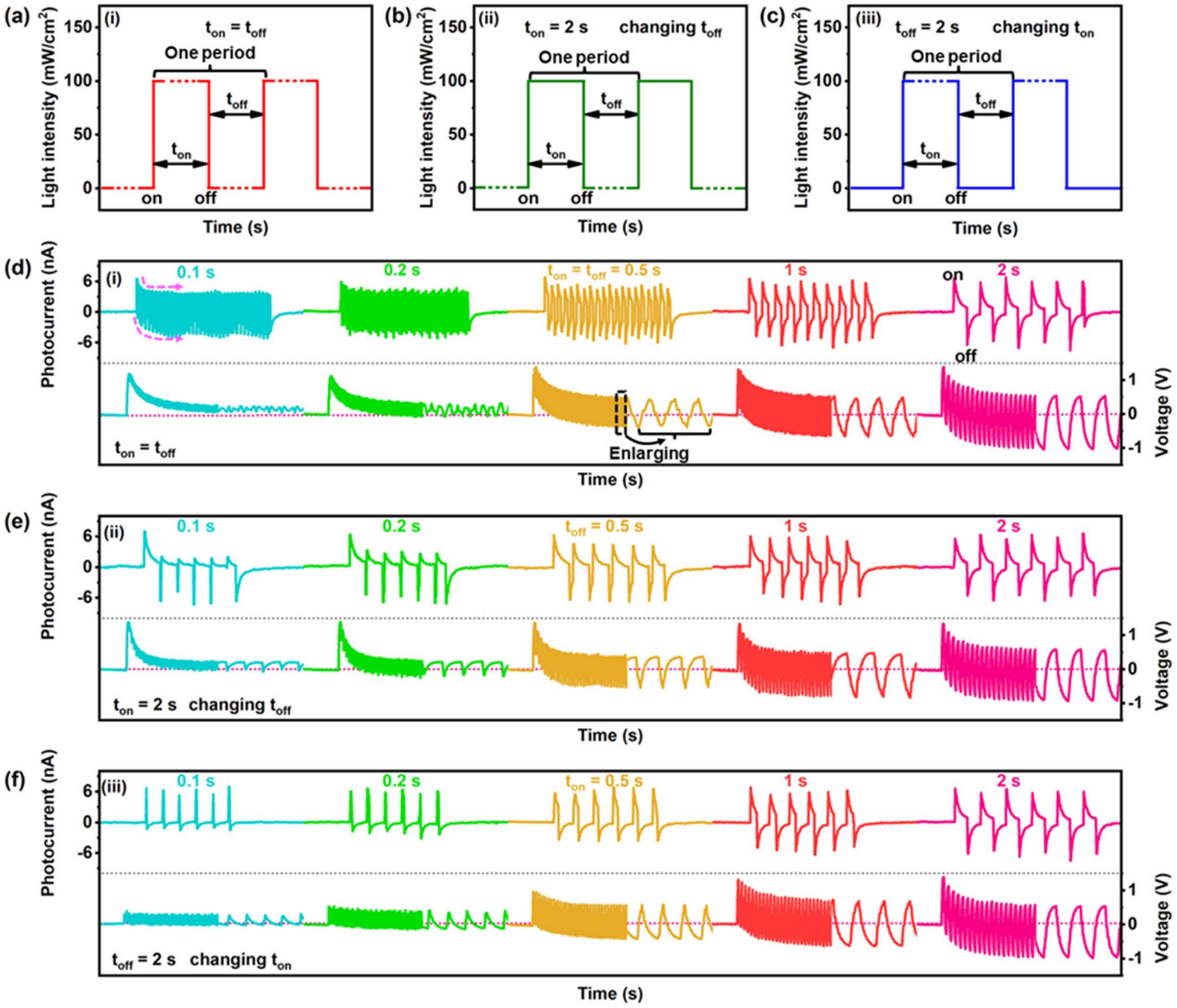

Fig. 5 Light turning on/off time-dependent photo-pyroelectric currents of the PVDF-10 film. Three kinds of periodic illumination conditions (a–c) and corresponding photo-pyroelectric response (d–f): (a) and (d) the light turning on/off time is the same. (b) and (e) Light turning on time (t_{on}) is fixed at 2 s, and the light turning off time (t_{off}) is changed. (c) and (f) Light turning off time (t_{off}) is fixed at 2 s, and the light turning on time (t_{on}) is changed. The solid lines and dashed lines in (a)–(c) mean that the time is fixed and changed, respectively. The used light is a 365 nm LED with a light intensity of 100 mW cm^{-2}.

zero at the first period. The net voltage is superposed in the next period (Fig. S14, ESI†). Until the temperature rise and dissipation reach dynamic equilibrium, the output voltage reaches maximum value of about 1.25 V. After the temperature becomes stable, the film polarization starts to achieve a new steady state. Thereby, the voltage slowly decreases and ultimately fluctuates around 0 V. Similar to I_{py}, the longer the period, the greater the temperature disturbance and the greater the ultimate output voltage, changing from 0.2/0 V to 0.5/−1.0 V.

In situation (ii): fixing t_{on} = 2 s and changing t_{off} (Fig. 5b and e). Due to the same starting temperature, the positive I_{py} is about 6 nA in the beginning of all the periods. However, under continuous illumination, the film temperature quickly becomes stable. The magnitude of temperature fluctuation when the light turns on positively depends on t_{off} (Fig. S15, ESI†). Therefore, the positive I_{py} gradually increases from 2 nA to 6 nA with the increase in t_{off} from 0.1 s to 2 s. By contrast, the dT/dt at the moment turning the light off is almost identical, resulting in the equal negative I_{py} of −6 nA. Due to $t_{off} \le t_{on}$ in this situation, the voltage change is similar to that in situation (i). For situation (iii): fixing t_{off} = 2 s and changing t_{on} (Fig. 5c and f). When t_{on} < 1 s, the film temperature always remains at a low level (Fig. S16, ESI†). Although the dissipation speed is slow, the increasing temperature caused by light irradiation is enough to be dissipated after turning the light off, which results in that the film presents a large positive I_{py} of 6 nA but small negative I_{py} (−1.3 nA and −3.6 nA for t_o = 0.1 s and 0.5 s, respectively). Concurrently, the voltage almost restores to zero at the end of the initial period, but not superpose in the next period.

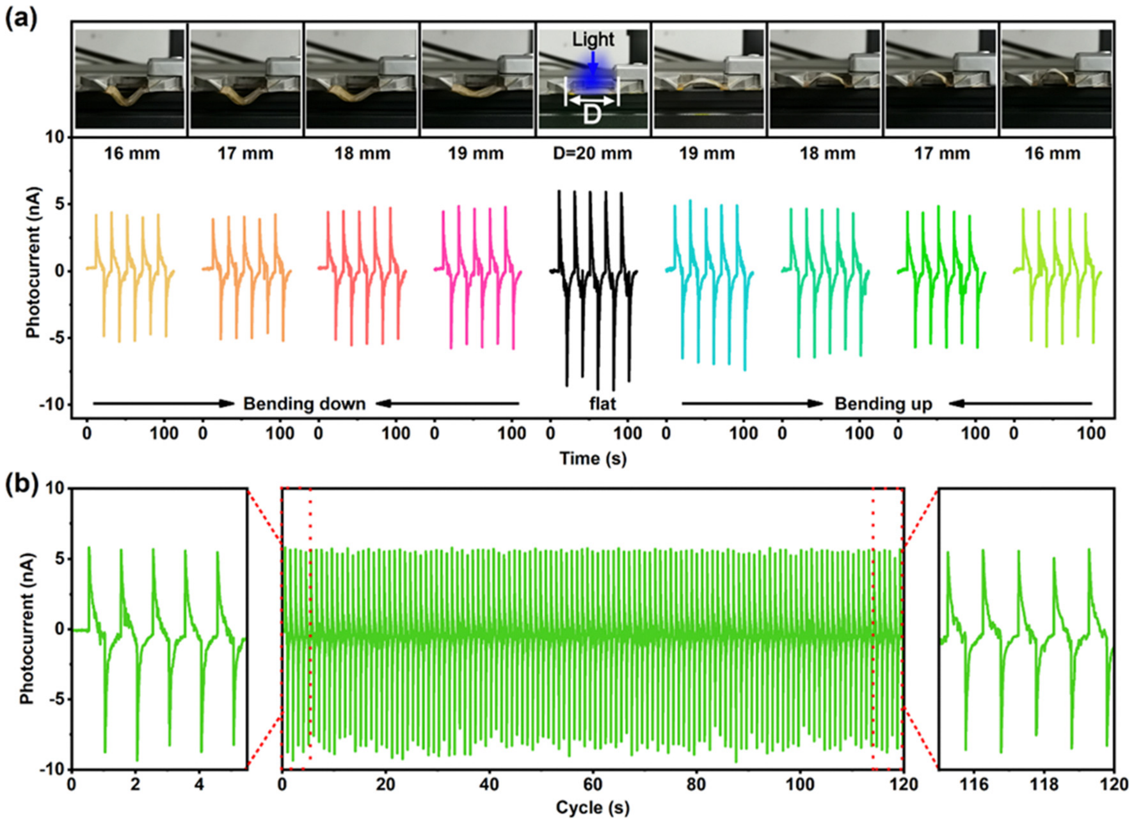

Fig. 6 Stability measurements of the photo-pyroelectric currents of the PVDF-10 film. The used light is a 365 nm LED with a light intensity of 100 mW cm^{-2}. (a) Top photos present the PVDF-10 films with different degrees of bending. The bottom curves are the photo-pyroelectric current corresponding to the top bending films. (b) Cycling stability of the PVDF-10 film under periodic light illumination.

Therefore, when t_{on} < 1 s, the maximum voltage in this situation is lower than that in situation (ii) and (iii). With extending the t_{on}, the film temperature increases, making the dissipation during light off faster, thus the negative I_{py} increases to about −6 nA. The voltage change starts to tend to situation (i) and (ii). In summary, the waveform, pulse width and amplitude of the output signals are easily manipulated by regulating t_{on} and t_{off}, which will largely extend the application of the pyroelectric films.

Under some conditions, the film needs to be bent to satisfy the specific demands. The photo-pyroelectric current under different degrees of bending is tested (Fig. 6a). It is found that after greatly bending, when the distance between the two terminals of the film decreases from 20 cm to 16 cm, the positive I_{py} changes from 6 nA to 4.2 nA (bending down) and 4.7 nA (bending up), which are 71% and 80% of the flat film. The decline can be considered from the decreasing effective irradiation area of film after bending, as well as the changes in the light reflection and transmission coefficient induced by the changes in the angle of incident light. Besides, the I_{py} value does not show any deterioration after over 100 cycles (Fig. 6b), confirming excellent stability of the film under periodic illumination. The excellent photo-pyroelectric response, simple frequency adjustability and stability provide the PVDF composite film potential applications in photodetection, wearable devices, environmental monitoring and other fields.

4. Conclusions

Flexible ferroelectric composite films with excellent photodetection properties and favorable mechanical flexibility present noticeable prospects in wearable devices. In this work, we have successfully introduced a Mn-doped BZT-BCT (BZTM$_{0.12}$-BCT) composition with a narrow bandgap and a high pyroelectric coefficient into the PVDF film to boost its photo-pyroelectric response. The BZTM$_{0.12}$-BCT particles exhibit positive impact on the content of polar β phase, crystallinity and photothermal conversion ability of the PVDF film, which jointly boost the photo-pyroelectric output. When the BZTM$_{0.12}$-BCT content is 10 wt%, the composite film presents the optimal output current, significantly higher than that of the pure PVDF film. Furthermore, the output amplitude and waveform are easily manipulated by the periodic illumination frequency. Excellent stability under bending conditions and repeated periodic irradiations are confirmed. This work provides a potential candidate for the future self-powered applications. However, a higher photoelectric output and superior anti-environmental interference ability are required for ferroelectric films to meet the demand of self-powering and information accuracy in practical applications.

Data availability

The data supporting this article are included as part of the ESI.†

Author contributions

L. W. and Z. Y. proposed the experimental scheme. L. W., F. Y. and J. P. carried out the experiment. All authors analyzed and discussed the results. L. W. and Z. Y. edited the manuscript. All authors have given approval to the final version of the manuscript.

Conflicts of interest

There are no conflicts to declare.

Acknowledgements

This work was financially supported by the National Natural Science Foundation of China (Grant no. 52372130, 52202152 and 52250410356), the Natural Science Foundation of Shanghai (Grant no. 22ZR1471200); the Future Partner Special Project of the Chinese Academy of Sciences (Grant no. 030GJHZ2023 076FN), the Frontier Science Key Project of the Chinese Academy of Sciences (Grant no. QYZDB-SSW-JSC027) and the Instrument Developing Project of Chinese Academy of Sciences (Grant no. ZDKYYQ20180004).

References

1 K. Yao, S. Chen, S. C. Lai and Y. M. Yousry, *Adv. Sci.*, 2022, **9**, e2103842, DOI: 10.1002/advs.202103842.

2 H. Xue, L. Jiang, G. Lu and J. Wu, *Adv. Funct. Mater.*, 2022, **33**, 2212110, DOI: 10.1002/adfm.202212110.

3 M. Tian, L. Xu, H. Dan and Y. Yang, *Nanoscale Horiz.*, 2022, **7**, 1240–1249, DOI: 10.1039/D2NH00204C.

4 L. Su, T. Yan, X. Liu, F. Cao and X. Fang, *Adv. Funct. Mater.*, 2023, **33**, 2214533, DOI: 10.1002/adfm.202214533.

5 H. Zou, G. Dai, A. C. Wang, X. Li, S. L. Zhang, W. Ding, L. Zhang, Y. Zhang and Z. L. Wang, *Adv. Mater.*, 2020, **32**, e1907249, DOI: 10.1002/adma.201907249.

6 C. Paillard, X. Bai, I. C. Infante, M. Guennou, G. Geneste, M. Alexe, J. Kreisel and B. Dkhil, *Adv. Mater.*, 2016, **28**, 5153–5168, DOI: 10.1002/adma.201505215.

7 Y. Yuan, Z. Xiao, B. Yang and J. Huang, *J. Mater. Chem. A*, 2014, **2**, 6027–6041, DOI: 10.1039/C3TA14188H.

8 G. Huangfu, H. Xiao, L. Guan, H. Zhong, C. Hu, Z. Shi and Y. Guo, *ACS Appl. Mater. Interfaces*, 2020, **12**, 33950–33959, DOI: 10.1021/acsami.0c09991.

9 S. C. Lai, K. Yao and Y. F. Chen, *Appl. Phys. Lett.*, 2013, **103**, 092903, DOI: 10.1063/1.4819845.

10 K. Zhao, H. Zhang, J. Meng, C. C. Chung, B. N. Gu, M. J. Liu, D. Zhang, M. Zhong, M. Liu, N. Liu, C. J. Lin, C. Meng and Y. L. Chueh, *Adv. Funct. Mater.*, 2022, **32**, 2204234, DOI: 10.1002/adfm.202204234.

11 M. Kumar and H. Seo, *Adv. Mater.*, 2022, **34**, e2106881, DOI: 10.1002/adma.202106881.

12 S. Sahare, P. Ghoderao, M. K. Sharma, M. Solovan, R. Aepuru, M. Kumar, Y. Chan, M. Ziółek, S.-L. Lee and Z.-H. Lin, *Nano Energy*, 2023, **107**, 108172, DOI: 10.1016/j.nanoen.2023.108172.

13 H. Fang, C. Xu, J. Ding, Q. Li, J. L. Sun, J. Y. Dai, T. L. Ren and Q. Yan, *ACS Appl. Mater. Interfaces*, 2016, **8**, 32934–32939, DOI: 10.1021/acsami.6b10305.

14 H. Liu, T. Zhao, W. Jiang, R. Jia, D. Niu, G. Qiu, L. Fan, X. Li, W. Liu, B. Chen, Y. Shi, L. Yin and B. Lu, *Adv. Funct. Mater.*, 2015, **25**, 7071–7079, DOI: 10.1002/adfm.201502752.

15 N. Ma, K. Zhang and Y. Yang, *Adv. Mater.*, 2017, **29**, 1703694, DOI: 10.1002/adma.201703694.

16 Q. Leng, L. Chen, H. Guo, J. Liu, G. Liu, C. Hu and Y. Xi, *J. Mater. Chem. A*, 2014, **2**, 11940–11947, DOI: 10.1039/C4TA01782J.

17 J.-H. Lee, H. Ryu, T.-Y. Kim, S.-S. Kwak, H.-J. Yoon, T.-H. Kim, W. Seung and S.-W. Kim, *Adv. Energy Mater.*, 2015, **5**, 1500704, DOI: 10.1002/aenm.201500704.

18 K. Vinodan, S. K. Chacko, R. Mohammed, B. Raneesh, N. kalarikkal, T. Woldu and D. Rouxel, *Polymer*, 2023, **281**, 126135, DOI: 10.1016/j.polymer.2023.126135.

19 S. Jachalke, E. Mehner, H. Stöcker, J. Hanzig, M. Sonntag, T. Weigel, T. Leisegang and D. C. Meyer, *Appl. Phys. Rev.*, 2017, **4**, 021303, DOI: 10.1063/1.4983118.

20 H. Z. Li, W. Z. Li, Y. J. Yang, H. L. Tai, X. S. Du, R. Y. Gao and S. Y. Li, *Ceram. Int.*, 2018, **44**, 19254–19261, DOI: 10.1016/j.ceramint.2018.07.150.

21 W. Li, A. Zheng, Y. Lin, P. Liu, M. Shen, L. Zhou, H. Liu, J. Yuan, S. Qin, X. Zhang, N. Yang, S. Jiang and G. Zhang, *Mater. Lett.*, 2020, **267**, 127514, DOI: 10.1016/j.matlet.2020.127514.

22 B. Zhang, C. Guo, X. Cao, X. Yuan, X. Li, H. Huang, S. Dong, Z. L. Wang and K. Ren, *Nano Energy*, 2022, **104**, 107897, DOI: 10.1016/j.nanoen.2022.107897.

23 M. Yan, S. Liu, Y. Liu, Z. Xiao, X. Yuan, D. Zhai, K. Zhou, Q. Wang, D. Zhang, C. Bowen and Y. Zhang, *ACS Appl. Mater. Interfaces*, 2022, **14**, 53261–53273, DOI: 10.1021/acsami.2c15581.

24 H. Li, H. Wang, X. Li, J. Huang, X. Li, S. K. Boong, H. K. Lee, J. Han and R. Guo, *Nano Energy*, 2022, **100**, 107527, DOI: 10.1016/j.nanoen.2022.107527.

25 D. Zabek, J. Taylor, E. L. Boulbar and C. R. Bowen, *Adv. Energy Mater.*, 2015, **5**, 1401891, DOI: 10.1002/aenm.201401891.

26 J. Lee, H. J. Kim, Y. J. Ko, J. Y. Baek, G. Shin, J. G. Jeon, J. H. Lee, J. H. Kim, J. H. Jung and T. J. Kang, *Nano Energy*, 2022, **97**, 107178, DOI: 10.1016/j.nanoen.2022.107178.

27 L. Wang, F. Zhang, C. Chen, X. He, M. A. Boda, K. Yao and Z. Yi, *Nano Energy*, 2024, **119**, 109081, DOI: 10.1016/j.nanoen.2023.109081.

28 P. Martins, A. C. Lopes and S. Lanceros-Mendez, *Prog. Polym. Sci.*, 2014, **39**, 683–706, DOI: 10.1016/j.progpolymsci.2013.07.006.

29 C. Ribeiro, C. M. Costa, D. M. Correia, J. Nunes-Pereira, J. Oliveira, P. Martins, R. Goncalves, V. F. Cardoso and S. Lanceros-Mendez, *Nat. Protoc.*, 2018, **13**, 681–704, DOI: 10.1038/nprot.2017.157.

30 X. Qian, X. Chen, L. Zhu and Q. M. Zhang, *Science*, 2023, **380**, eadg0902, DOI: 10.1126/science.adg0902.

31 M. N. Islam, R. H. Rupom, P. R. Adhikari, Z. Demchuk, I. Popov, A. P. Sokolov, H. F. Wu, R. C. Advincula, N. Dahotre, Y. Jiang and W. Choi, *Adv. Funct. Mater.*, 2023, **33**, 2302946, DOI: 10.1002/adfm.202302946.

32 Y. Liu, Y. Zhou, H. Qin, T. Yang, X. Chen, L. Li, Z. Han, K. Wang, B. Zhang, W. Lu, L. Q. Chen, J. Bernholc and Q. Wang, *Nat. Mater.*, 2023, **22**, 873–879, DOI: 10.1038/s41563-023-01564-7.

33 K. Jeder, A. Bouhamed, H. Nouri, N. Abdelmoula, N. Jöhrmann, B. Wunderle, H. Khemakhem and O. Kanoun, *Energy*, 2022, **261**, 125169, DOI: 10.1016/j.energy.2022.125169.

34 T. Huang, S. Yang, P. He, J. Sun, S. Zhang, D. Li, Y. Meng, J. Zhou, H. Tang, J. Liang, G. Ding and X. Xie, *ACS Appl. Mater. Interfaces*, 2018, **10**, 30732–30740, DOI: 10.1021/acsami.8b10552.

35 R. Gregorio, *J. Appl. Polym. Sci.*, 2006, **100**, 3272–3279, DOI: 10.1002/app.23137.

36 L. Ruan, X. Yao, Y. Chang, L. Zhou, G. Qin and X. Zhang, *Polymers*, 2018, **10**, 228, DOI: 10.3390/polym10030228.

37 C.-M. Wu, M.-H. Chou, T. F. Chala, Y. Shimamura and R.-I. Murakami, *Compos. Sci. Technol.*, 2019, **178**, 26–32, DOI: 10.1016/j.compscitech.2019.05.004.

38 F. Khan, T. Kowalchik, S. Roundy and R. Warren, *Scr. Mater.*, 2021, **193**, 64–70, DOI: 10.1016/j.scriptamat.2020.10.036.

39 A. Ferri, S. Barrau, R. Bourez, A. Da Costa, M. H. Chambrier, A. Marin, J. Defebvin, J. M. Lefebvre and R. Desfeux, *Compos. Sci. Technol.*, 2020, **186**, 107914, DOI: 10.1016/j.compscitech.2019.107914.

40 A. Magnani, S. Capaccioli, B. Azimi, S. Danti and M. Labardi, *Polymers*, 2022, **14**, 5379, DOI: 10.3390/polym14245379.

41 T. Zhao, W. Jiang, H. Liu, D. Niu, X. Li, W. Liu, X. Li, B. Chen, Y. Shi, L. Yin and B. Lu, *Nanoscale*, 2016, **8**, 8111–8117, DOI: 10.1039/C5NR09290.